

Shock Wave Response of Porous Materials: From Plasticity to Elasticity

Aiguo Xu, Guangcai Zhang, Yangjun Ying, Ping Zhang and
Jianshi Zhu

National Key Laboratory of Computational Physics,
Institute of Applied Physics and Computational Mathematics, P. O. Box 8009-26,
Beijing 100088, P.R.China
E-mail: Xu_Aiguo@iapcm.ac.cn

Abstract. Shock wave reaction results in various characteristic regimes in porous material. The geometrical and topological properties of these regimes are highly concerned in practical applications. Via the morphological analysis to characteristic regimes with high temperature, we investigate the thermodynamics of shocked porous materials whose mechanical properties cover a wide range from hyperplasticity to elasticity. It is found that, under fixed shock strength, the total fractional area A of the high-temperature regimes with $T \geq T_{th}$ and its saturation value first increase, then decrease with the increasing of the initial yield σ_{Y0} , where T_{th} is a given threshold value of temperature T . In the shock-loading procedure, the fractional area $A(t)$ may show the same behavior if T_{th} and σ_{Y0} are chosen appropriately. Under the same $A(t)$ behavior, T_{th} first increases then decreases with σ_{Y0} . At the maximum point σ_{Y0M} , the shock wave contributes the maximum plastic work. Around σ_{Y0M} , two materials with different mechanical properties may share the same $A(t)$ behavior even for the same T_{th} . The characteristic regimes in the material with the larger σ_{Y0} are more dispersed.

1. Introduction

Porous materials are ubiquitous in nature and extensively used as industrial materials. Examples are referred to wood, bricks, metals, foams, ceramics, carbon and explosives. The use of porous materials in parts may lead to reduced weight, improved structural and mechanical properties, better heat transfer, greater motion and deformation control, etc[1, 2]. Besides others, they have also been used in surgical implant design to fabricate devices to replace or augment soft and hard tissues[3, 4]. Although the study on shock wave reaction on porous materials has a long history. Most of previous studies were focussed on the global behaviors, such as the Hugoniot[5, 6, 7, 8, 9, 10, 11, 12] and the equation of state[13, 14, 15]. The dynamical procedures involve much richer physical behaviors but in fact are much less extensively investigated.

The main challenges for studying the dynamical behaviors in shocked porous material are twofold: the first is the numerical tool, the second is the scheme to analyze the simulation data. From the simulation side, an appropriate simulation tool must overcome two constraints. The first is the scale limitation. Molecular dynamics can discover some atomistic mechanisms of shock-induced void collapse[16, 17], but the spatial and temporal scales it may cover are far from being comparable with experiments. To overcome the scale limitation, one solution is to develop some mesoscopic particle methods. The second constraint is the numerical stability. Traditional simulation methods, both the Eulerian and Lagrangian ones, when treating with the dynamics of structured and/or porous materials, encountered severe difficulties. The reason is that material under investigation is generally highly distorted during the collapsing of cavities. The Eulerian description is not convenient for tracking interfaces. Lagrangian formulation has to rezone the meshes to restore proper shapes. The mapping of state fields of mass density, velocities and stresses from the distorted mesh to the newly generated one is not easy and introduces errors. In this study we use a mixed method, material-point method(MPM)[18, 19], to study shock wave reaction on porous materials. As a step to approach the shock wave dynamics in porous materials, we have carefully studied the cavity collapse in shocked materials[19, 20].

As for the second challenge, data analysis and information picking up, a relatively straightforward way is to study the local averaged values and the corresponding fluctuations of state variables[21]. In Ref.[21], the evolution of local turbulence mixing and volume dissipation were also studied. Shock wave reaction results in various characteristic regimes in porous materials, for example, regimes with high temperature, regimes with high pressure, regimes with high particle speeds, etc. These characteristic regimes are generally highly concerned in practical applications. Regimes with high temperature are places where initiation may start in energetic materials. Regimes with high pressure are places where phase transition may occur. Regimes with high particle speed are places where jet phenomena may occur. To understand the characteristic regimes defined by $\Theta \geq \Theta_{th}$, we[22] introduced the Minkowski functionals to measure their morphological behaviors, where Θ is a physical variable under consideration, like

the temperature, density, some specific stress, particle velocity or its components, Θ_{th} a given threshold value.

Previous studies showed that the porous metal aluminum(Al)[22] and porous HMX-like material[23] show significant differences under shock wave reaction. To clarify the effects of single material parameters and present indicative information for material designs, it is interesting to have a through study on the shock behaviors in relation to their mechanical property ranging from hyper-plastic to pure elastic[24].

In present paper we focus on characteristic regimes with high temperature. We organize the following part of the paper as follows. Section 2 briefly introduces the material model and the numerical method. Section 3 outlines the morphological characterization for characteristic regimes manifested by Turing patterns. Simulation results are shown and analyzed in section 4. Section 5 makes the conclusion.

2. Material model and material-point method

The porous material is fabricated by a solid body with a number of randomly distributed voids embedded. The solid body follows an associative von Mises plasticity model with linear kinematic and isotropic hardening[21]. The pressure P is calculated by using the Mie-Grüneissen equation of state which can be written as $P - P_H = [\gamma(V)/V][E - E_H(V_H)]$, where P_H , V_H and E_H are pressure, specific volume and energy on the Rankine-Hugoniot curve, respectively. The relation between P_H and V_H can be estimated by experiments and be written as

$$P_H = \begin{cases} \frac{\rho_0 c_0^2 (1 - \frac{V_H}{V_0})}{(\lambda - 1)^2 (\frac{\lambda}{\lambda - 1} \times \frac{V_H}{V_0} - 1)^2}, & V_H \leq V_0 \\ \rho_0 c_0^2 (\frac{V_H}{V_0} - 1), & V_H > V_0 \end{cases} \quad (1)$$

where ρ_0 , V_0 are the initial density and specific volume of the solid material, c_0 the sound speed, λ the coefficient in Hugoniot velocity relation. Both the shock compression and the plastic work $E - E_H(V_H)$ cause the increasing of temperature. The increasing of temperature from shock compression can be calculated as:

$$\frac{dT_H}{dV_H} = \frac{c_0^2 \cdot \lambda (V_0 - V_H)^2}{c_v [(\lambda - 1)V_0 - \lambda V_H]^3} - \frac{\gamma(V)}{V_H} T_H. \quad (2)$$

where c_v is the specific heat. Eq.(2) can be derived from the thermal equation and the Mie-Grüneissen equation of state[21]. The increasing of temperature from plastic work can be calculated as: $dT_p = dW_p/c_v$.

We model shocked materials with continuously varying mechanical properties. The reference material is the metal aluminum. The corresponding parameters are as below: density in solid portion $\rho_0 = 2700 \text{ kg/m}^3$, Yang's module $E = 69 \text{ Mpa}$, Poisson's ratio $\nu = 0.33$, initial yield $\sigma_{Y0} = 120 \text{ Mpa}$, tangential module $E_{\text{tan}} = 384 \text{ MPa}$, sound speed $c_0 = 5.35 \text{ km/s}$, characteristic coefficient in the Hugoniot velocity relation $\lambda = 1.34$, specific heat $c_v = 880 \text{ J/(Kg}\cdot\text{K)}$, heat conduction coefficient $k = 237 \text{ W/(m}\cdot\text{K)}$, and Grüneissen coefficient $\gamma = 1.96$. The initial temperature of the material is 300 K. In simulations a wide range of the yield σ_{Y0} will be used.

The material point method is a relatively new particle method in computational solid mechanics. This method uses a regular structured grid as a computational scratchpad for computing spatial gradients of field variables. The grid is convected with the particles during deformations that occur over a time step, eliminating the diffusion problems associated with advection on an Eulerian grid. The grid is restored to its original location at the end of a time step. In addition to avoiding the Eulerian diffusion problem, this approach also circumvents problems with mesh entanglement that can plague fully Lagrangian-based techniques when large deformations are encountered. The MPM has also been successful in solving problems involving impact, etc. It has an advantage over traditional finite element methods in that the use of the regular grid eliminates the need for doing costly searches for contact surfaces. Details of the scheme is referred to our previous publications[19, 18].

3. Outline of morphological description

A variety of techniques can be used to describe the complex spatial distribution and time evolution of physical quantities in the shocked porous material. In this study we concentrate on the set of statistics known as Minkowski functionals[25, 26, 27]. The Minkowski functionals has been successfully used to characterize patterns in reaction-diffusion systems[28], spinodal decomposition[29, 30], fluctuations of cosmic microwave background[31], block copolymer systems[32, 33] and to reconstruct complex materials[34].

Assume Θ is a physical quantity being interesting to us, then the regions with $\Theta \geq \Theta_{th}$ in the shocked porous material are referred to as characteristic regimes, where Θ_{th} is a threshold value of Θ . To simplify the analysis of the complex physical field, we first condense the physical field as two kinds of characteristic regimes, the white and the black. The white correspond to regimes with $\Theta \geq \Theta_{th}$ and the black correspond to regimes with $\Theta < \Theta_{th}$. For such Turing patterns, a general theorem of integral geometry states that all properties of a d -dimensional convex set which satisfy motion invariance and additivity (called morphological properties) are contained in $d + 1$ numerical values [35]. For a condensed temperature field, the white correspond to the high-temperature regimes and the black correspond to the low-temperature regimes. The high-temperature regimes are also generally referred to “hot-spots”.

For a two-dimensional temperature map, the three Minkowski functionals correspond geometrically to the total fractional area A of the high-temperature regimes, the boundary length L between the high- and low-temperature regimes per unit area, and the Euler characteristic χ per unit area (equivalent to the topological genus). When we increase the temperature threshold T_{th} from the lowest temperature to the highest one, the high-temperature area A will decrease from 1 to 0; the boundary length L first increases from 0, then arrives at a maximum value, finally decreases to 0 again. There are several ways to define the Euler characteristic χ . Two simplest one is $\chi = (N_W - N_B)/N$, where N_W (N_B) is the number of connected white (black)

Figure 1. (Color online) Snapshots of shocked porous material, where $\Delta = 0.5$, $v_{init} = 1000$ m/s, $t=1000$ ns, . From left to right and from top to bottom, the initial yields in the two rows are $\sigma_{Y0} = 12, 120, 3000, 8000, 10000, 12000, 15000, 20000$ Mpa, respectively. The unit of length is $10\mu\text{m}$. The width and height of the simulated system are 1mm and 5mm, respectively. From blue to red the color corresponds to increase of temperature.

regimes, N is the total number of pixels. In contrast to the area A and boundary length L , the Euler characteristic χ describes the connectivity of the characteristic regimes in the material. It describes the patterns in a purely topological way, i.e., without referring to any kind of metric. It is negative (positive) if many disconnected black (white) regimes dominate the image. A vanishing Euler characteristic indicates a highly connected structure with equal amount of black and white regimes. The ratio $\kappa = \chi/L$ describes the mean curvature of the boundary line separating black and white regimes. More discussions and calculation schemes of the Minkowski functionals are referred to Refs.[26, 28, 36].

Among the three Minkowski functionals, the high-temperature area A is the only one which monotonically increases in the shock-loading procedure and/or when the threshold value becomes smaller. For a given T_{th} , its increasing rate, D , presents meaningful information. When the temperature threshold T_{th} becomes higher, D decreases. The variations of A , L and χ with T_{th} and time t compose a scenario for the shock response of porous material[22].

4. Simulation results and physical interpretation

If denote the mean density of the porous body as ρ , then the porosity of the material is $\Delta = 1 - \rho/\rho_0$ [37]. The shock to target body is loaded by colliding with a rigid wall being static at the bottom position $y = 0$. The initial velocity of the porous body is $-v_{init}$. The collision starts at time $t = 0$. The height and width of the porous body are 5mm and 1mm, respectively. Periodic boundary conditions are used in the horizontal directions, which means that the real system is composed of many of the simulated ones aligned periodically in the horizontal direction.

4.1. Case with $v_{init} = 1000$ m/s

Figure 1 presents a series of snapshots in the shock loading procedure, where the porosity $\Delta = 0.5$ and initial velocity $v_{init} = 1000\text{m/s}$, the time $t = 1000\text{ns}$. From left to right and from top to bottom, the two rows of snapshots are for cases with $\sigma_{Y0} = 12, 120, 3000, 8000, 10000, 12000, 15000, 20000$ Mpa, respectively. The points in the figure correspond to the material particles. The color from blue to red corresponds to increasing of temperature. From Fig.1 one can find the moving down of upper free surface and moving up of global compressive-waves series. For each case, the initial shock wave is decomposed as a complex series of compressive and rarefactive waves. In the shock

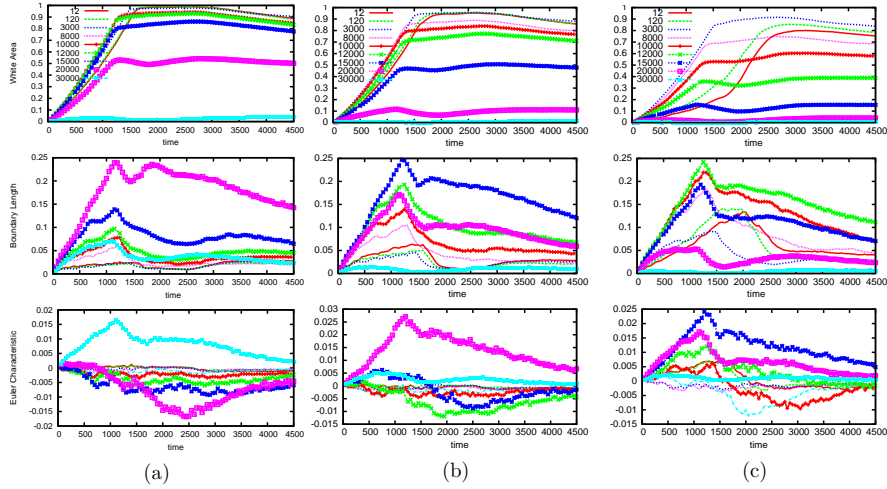


Figure 2. (Color online) Minkowski measurements for cases with various initial yields, where $\Delta = 0.5$, $v_{init} = 1000$ m/s. The values of σ_{Y0} are shown in the legend with the unit MPa. $T_{th} = 400\text{K}$ in (a), $T_{th} = 500\text{K}$ in (b), $T_{th} = 600\text{K}$ in (c).

loading procedure, the compressive effects dominate. Within the shocked region, both the plastic work and shock compression make the temperature increase. In the present case, the plastic work dominates. The high-temperature regimes in materials with higher initial yields are more dispersed. The increasing rate of high-temperature area $A(t)$ is different when the initial yield changes.

To quantify and get a more complete understanding on the shock wave response behavior, we show a set of morphological measures versus time in Fig.2(a), where values of initial yields are shown in the legend. The temperature threshold here is $T_{th} = 400$ K. With the propagation of compressive-wave-series in the porous material, the high-temperature area A first increases with time in a parabolic way, then approaches to a saturation value slowly, keeps the saturation value for a period, finally decreases. The final decrease indicates that rarefactive waves are reflected back from the upper free surface and are decreasing the mean pressure and temperature, an amount of material particles changed their temperature from $T > T_{th}$ to $T < T_{th}$. During the saturation period, more compressive waves arrived at the upper free surface, consequently, more rarefactive waves are reflected back into the porous body. The former tends to increase the temperature, while the latter tends to decrease. The two effects are nearly balanced. Therefore, the high-temperature area A keeps nearly a constant.

As for effects of the initial yield σ_{Y0} , we can find two interesting phenomena: Both the initial increasing rate and the saturation value of A first increase, then decrease when the material changes from being superplastic to pure elastic. For cases checked in our numerical experiments, the increasing rate D becomes larger when the initial yield σ_{Y0} increases from 0 to about 10 Gpa. If σ_{Y0} further to increase, D will decrease. The saturation value A_S of high-temperature area becomes larger when σ_{Y0} increases from being very small to about 1 Gpa. When σ_{Y0} becomes larger, the saturation value A_S

decreases. For the time interval shown Fig. 2(a), when $\sigma_{Y0} > 10$ Gpa, the saturation value A_S decreases and the period for $A \approx A_S$ becomes shorter with the increasing of σ_{Y0} . When $\sigma_{Y0} = 12$ Gpa, $A \approx 0.96$ during the period $1430 \text{ ns} < t < 2924 \text{ ns}$; When $\sigma_{Y0} = 15$ Gpa, A increases slowly from 0.8 to 0.86 during the period $1245 \text{ ns} < t < 2825 \text{ ns}$; When $\sigma_{Y0} = 20$ Gpa, $A_S \approx 0.52$ and have a local minimum value 0.49 at about $t = 1863 \text{ ns}$. When $\sigma_{Y0} = 30$ Gpa, the area A keeps very small.

Now we check the information given by the boundary length and Euler characteristic in Fig.2(a). For all cases shown in the figure, the boundary length L first increases, then decreases with time. The former increase corresponds to the propagation of compressive waves and the appearance of more hot-spots. The decreasing of $L(t)$ is not monotonic. The initial decrease corresponds to the coalescence of some hot-spots, the latter decrease corresponds to the coming in of the global rarefactive waves from the upper free surface, which result in expanding and coalescence of some cold-spots. A prominent behavior here is that, for the case with $\sigma_{Y0} = 20$ Gpa, the boundary length L has the largest value. For this case, the value of χ changes from being slightly positive to being the most negative. Combining information of A , L and χ , we can know that, with the propagation of compressive wave in the porous material, the number of hot-spots with $T > 400\text{K}$ quickly increases, but distributes quite scatteredly. After corresponding compressive wave scanned all the material body, some scattered cold-spots with $T < 400\text{K}$ expand and partly coalescence due to the coming in of rarefactive waves. During this procedure, some small hot-spots with $T > 400\text{K}$ disappear. Therefore, both the high-temperature area A and boundary length L decrease and the Euler Characteristic χ becomes more negative. For other cases, the smaller the boundary length L , the flatter the wave front in the temperature map. The material with $\sigma_{Y0} = 15$ Gpa has the secondary maximum boundary length L and more flatter $\chi(t)$ curve than the material with $\sigma_{Y0} = 20$ Gpa. This means that the numbers of hot-spots and cold-spots do not have much difference. The number of cold-spots dominates slightly during the time interval shown in the figure.

In the shock loading procedure, if we decrease the threshold value T_{th} , the wave fronts in the pixelized temperature map becomes flatter. Consequently, the values of $L(t)$ are smaller, the $\chi(t)$ values are closer to zero, and the curves for $A(t)$ becomes closer to be linear. If we increase the threshold value T_{th} , the pixelized temperature map shows different geometric and topological behaviors. Examples are referred to Figs. 2(b) and 2(c). $T_{th} = 500\text{K}$ in Fig. 2(b) and $T_{th} = 600\text{K}$ in Fig. 2(c). It is clear that the saturation values of $A(t)$ decrease with the increasing of T_{th} . In the shock-loading procedure, the material with $\sigma_{Y0} = 12$ Mpa has about 20% of material particles can not get a temperature higher than 600K and 5% can not get the temperature higher than 500K, and only 1% can not get the temperature higher than 400K. For the material with $\sigma_{Y0} = 120$ Mpa, in the shock loading procedure, there are about 15% of material particles can not get the temperature higher than 600K, 4% can not get the temperature higher than 500K, and only 1% can not get the temperature higher than 400K.

When the initial yield is very high, for example, $\sigma_{Y0} = 15\text{Gpa}$, the material is very elastic. Consequently, the saturation value A_S of high-temperature area is small. For

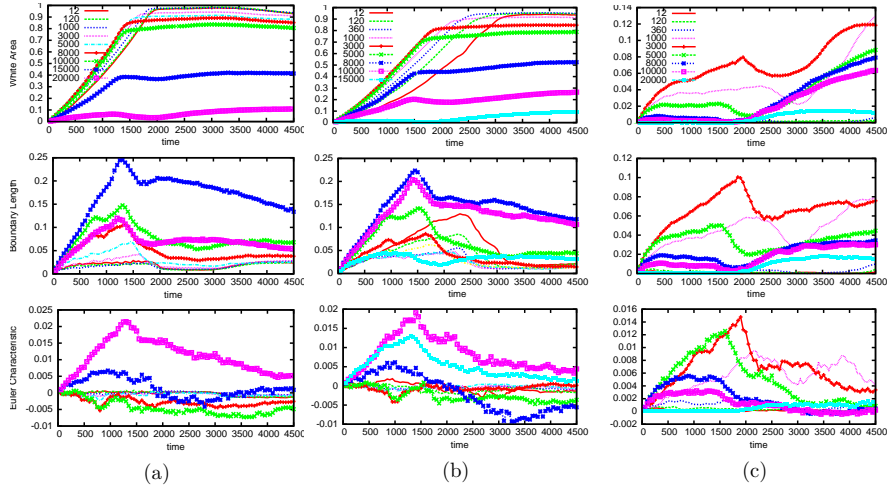


Figure 3. (Color online) Minkowski measurements for cases with various initial yields, where $\Delta = 0.5$. The values of σ_{Y0} are shown in the legend with the unit MPa. The threshold temperature is 400K. $v_{init} = 800$ m/s in (a), $v_{init} = 600$ m/s in (b), $v_{init} = 400$ m/s in (c).

example, $A_S = 0.15$ when $T_{th} = 600$ K, which means that 85% of material particles can not get the temperature higher than 600K. For the case with $\sigma_{Y0} = 20$ Gpa, $A_S = 0.54$ when $T_{th} = 400$ K, $A_S = 0.11$ when $T_{th} = 500$ K and $A_S = 0.04$ when $T_{th} = 600$ K. For the case with $\sigma_{Y0} = 30$ Gpa, only 0.1% of material particles can get a temperature higher than 600K in the shock loading procedure. In the temperature pattern with $T_{th} = 400$ K, the case of $\sigma_{Y0} = 20$ GPa has a largest boundary length. When $T_{th} = 500$ K, the case of $\sigma_{Y0} = 15$ GPa has a largest boundary length. When $T_{th} = 600$ K, the case of $\sigma_{Y0} = 10$ GPa has the largest L .

4.2. Effects of initial shock strength

With the decreasing of initial shock strength, both the highest and the mean temperatures in the shocked portion decrease. A set of Minkowski measures for the shocking procedure of porous materials with various initial yields are shown in Fig.3, where $\Delta = 0.5$ and $T_{th}=400$ K. The initial impact velocities are different in Figs. (a), (b) and (c). They are 800m/s, 600m/s and 400m/s, respectively. The values of initial yields are shown in the legends. Specifically, the initial yields are 12, 120, 1000,3000, 5000, 8000, 10000, 15000 and 20000MPa in Fig.3(a) ; in Fig.3(b) they are 12, 120, 360, 1000,3000, 5000, 8000, 10000 and 15000MPa; in Fig.3(c) they are 12, 120, 360, 1000,3000, 5000, 8000, 10000, and 20000MPa. Compared with cases shown in Fig. 2(a), both the saturation value A_S and the increasing rate $D(T_{th})$ of the high-temperature area decrease when the initial shock becomes weaker. As an example, for the material with $\sigma_{Y0} = 1000$ Mpa, when the initial impact velocity is $v_{init} = 1000$ m/s, there are 99% of material particles arrive at the temperature higher than 400K in the shock-loading procedure; when $v_{init} = 800$ m/s, the fraction of material particles getting the

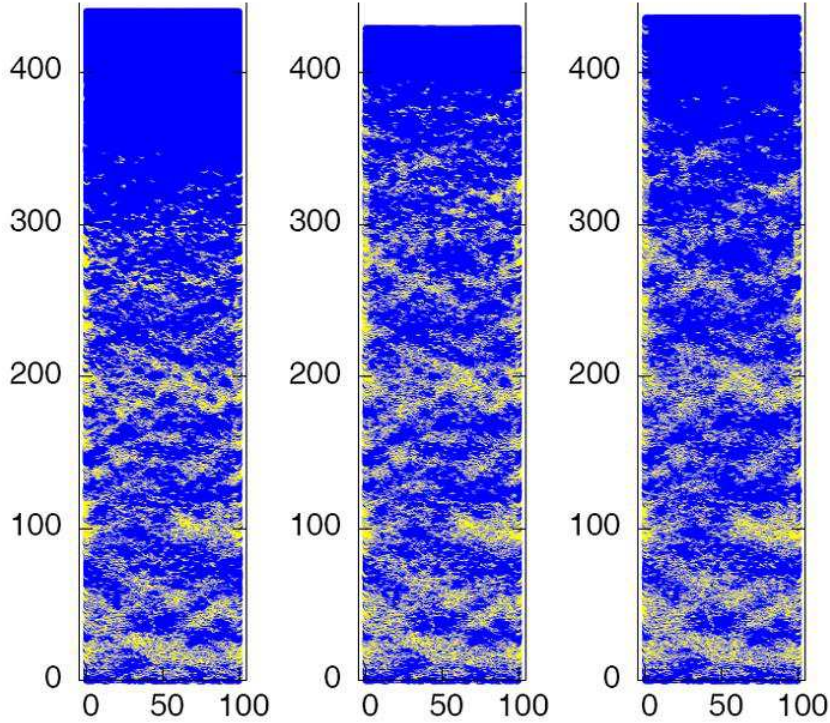


Figure 4. (Color online) Configurations with condensed temperature map, where $\Delta = 0.5$, $v_{init} = 400$ m/s, $\sigma_{Y0} = 3000$ Mpa. The areas with temperature higher than 400K are shown in yellow, other areas are in blue. The times corresponding to the three snapshots are 1500ns, 2000ns and 2500ns, respectively, from which one can find that the high-temperature area at $t=2000$ ns is a little larger than that at $t=2500$ ns and that at $t=1500$ ns.

temperature higher than 400K is 97%; when $v_{init} = 600$ m/s, the fraction is 89% ; when $v_{init} = 400$ m/s, the fraction becomes only 5%.

In Fig.3(c), the case of $\sigma_{Y0} = 3000$ MPa has the maximum high-temperature area A , boundary length L and Euler characteristic χ . In this figure, only after the high-temperature area A gets its maximum value, it begins to decrease, which means that, under such a shock strength, most material particles can not get a temperature higher than 400K, the threshold value 400K has been very close to the highest temperature in this system. To understand better why the maximum high-temperature area occurs at about $t=2000$ ns, we show the configurations with condensed temperature map in Fig.4, where the three snapshots are for the times $t=1500$ ns, 2000ns and 2500ns, respectively. The areas with temperature higher than 400K are shown in yellow, other areas are shown in blue. One can find that the high-temperature area at time $t=2000$ ns is the largest among the three snapshots. From the heights of the upper free surface, one can find that the one for $t=2000$ ns is the lowest, which means that the shock-loading procedure finishes at about that time. When the unloading procedure starts, the area with high-temperature decreases. From Fig.4 one can also find that the high-temperature regimes for $T_{th} = 400$ K have been very dispersed. This is consistent with the large value of boundary length, and consistent with the above observation that only a small portion of

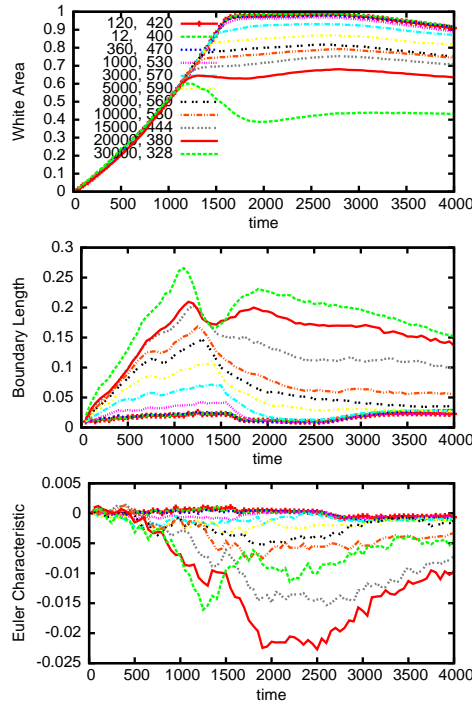


Figure 5. (Color online) Minkowski measurements versus time, where $\Delta = 0.5$, $v_{init} = 1000$ m/s, the values of σ_{Y0} and T_{th} are shown in the two columns of the legend. The units are MPa and K, respectively.

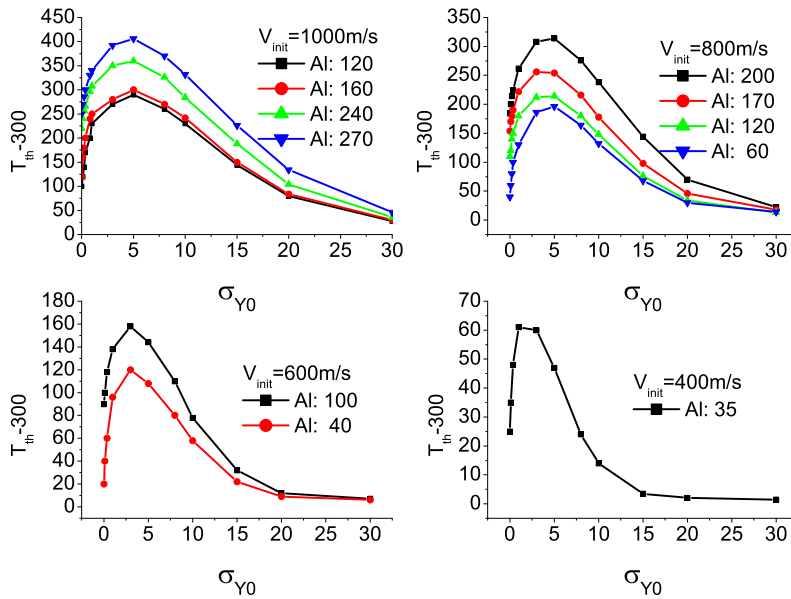


Figure 6. (Color online) T_{th} versus σ_{Y0} for the same $A(t)$ behavior. The initial impact velocities are shown in the legends. Each curve in the figure is labeled by the T_{th} value for the reference material, aluminum (Al). The units for the horizontal and vertical axes are GPa and K, respectively.

material particles get the temperature higher than 400K under such a shock strength.

4.3. (σ_{Y0}, T_{th}) pairs for the same $A(t)$ behavior

As mentioned above, among the three Minkowski functionals, the high-temperature area $A(t)$ is the only one being monotonic when the threshold value T_{th} decreases and/or with the going on of the shock-loading procedure. It is natural to check if $A(t)$ shows the same behavior when using appropriate (σ_{Y0}, T_{th}) pairs. Figure 5 shows such examples for the case with initial impact velocity $v_{init} = 1000\text{m/s}$. In Fig.5, the temperature threshold for reference material, aluminum, is 420K. From Fig. 5 we can find that materials with different initial yields, if we choose an appropriate T_{th} to observe, the high-temperature area $A(t)$ shows the same behavior in the shock-loading procedure. Such a property can be understood better by observing Figs. 1 and 4. From Figs. 1 and 4, it is also clear that, for a fixed shock strength, with the increasing of the initial yield, the wave front becomes wider, the high-temperature regimes becomes more scattered, more low-temperature domains are embedded in the compressed portion. This morphological behavior is manifested by larger boundary lengths and more negative Euler characteristics in Fig.5.

If use the (σ_{Y0}, T_{th}) pairs in Fig.5 as coordinates, we get the curve labeled by “ $V_{init}=1000\text{m/s}$ ” and “Al: 120” in Fig.6. For the shock strength $v_{init} = 1000\text{m/s}$, the material with $\sigma_{Y0} = 5\text{GPa}$ has the maximum T_{th} which is about 590K. In this case, the shock contributes the maximum plastic work and the system has the highest temperature. If increase the temperature threshold T_{th} to 460K, 540K and 570K, we have the other three curves. Along each of them, $A(t)$ shows the same behavior in the shock-loading procedure. If decrease the shock strength to $v_{init} = 800\text{m/s}$, 600m/s and 400m/s , we get the other three plots of Fig.6. The maximum value point σ_{Y0M} moves towards the lower value of the initial yield when the shock wave becomes weaker. In the shock loading procedure, if we decrease the threshold value T_{th} , the wave fronts becomes flater. Consequently, $L(t)$ curves become smaller, $\chi(t)$ becomes closer to zero; the curves for $A(t)$ becomes closer to be linear.

5. Conclusion

Shock wave reaction results in various characteristic regimes in porous materials. The properties of these regimes are highly concerned in practical applications. Based on the material-point simulation and morphological characterization, we investigate how the initial yield influence the behavior of high temperature regimes in shocked porous material. It is found that, under fixed shock strength, the total fractional area A of high-temperature regimes (with $T \geq T_{th}$) and its saturation value first increase, then decrease when initial yield σ_{Y0} becomes higher. In the shock-loading procedure the fractional area $A(t)$ may show the same behavior under various choices of T_{th} and σ_{Y0} . For the same $A(t)$ behavior, T_{th} first increases then decreases when σ_{Y0} becomes higher. At the maximum

point σ_{Y0M} , the plastic work by the shock gets the maximum value. Around σ_{Y0M} , two materials with different mechanical properties may share the same $A(t)$ behavior even for the same threshold T_{th} . The high-temperature regimes in the material with the higher initial yield σ_{Y0} are more dispersed. Other kinds of characteristic regimes, for example, those with high pressure, high particle speed, etc., can be studied in the same way.

Acknowledgments

A. Xu is grateful to Prof. Hua Li for helpful discussions on shock waves and porous materials, to Drs. G. Gonnella, A. Lamura and V. Sofonea for helpful discussions on morphological description. This work is supported partly by Science Foundations of Laboratory of Computational Physics, China Academy of Engineering Physics [under Grant Nos. 2009A0102005, 2009B0101012], and National Science Foundation of China (under Grant Nos.10702010, 10775018 and 10604010).

References

- [1] S. Nemat-Nasser and M. Hori, *Micromechanics: Overall Properties of Heterogeneous Materials* Second Revised Edition, Elsevier Science Press, 1999.
- [2] V. F. Nesterenko, *Dynamics of Heterogeneous Materials*, Springer-Verlag, New York, 2001.
- [3] M. Lundberg, B. Skårman, F. Cesar, L. R. Wallenberg, *Microporous and Mesoporous Materials*, **54** 97 (2002).
- [4] G. Lu, G.Q.M. Lu, and Z.M. Xiao, *J. Porous Materials* **6**, 359 (1999).
- [5] R. K. Linde and D. N. Schmidt, *J. Appl. Phys.* **37**, 3259 (1966).
- [6] R. R. Boade, *J. Appl. Phys.* **40**, 3781 (1969).
- [7] B. M. Butcher, *J. Appl. Phys.* **45**, 3864 (1974).
- [8] S. Bonnan and P. L. Hereil, *J. Appl. Phys.* **83**, 5741 (1998).
- [9] G. T. Gray III, N. K. Bourne and J. C. F. Milet, *J. Appl. Phys.* **94**, 6430 (2003).
- [10] A. D. Resnyansky, N. K. Bourne, *J. Appl. Phys.* **95**, 1760 (2004).
- [11] D. J. Pastine, M. Lombardi, A. Chatterjee and W. Tchen, *J. Appl. Phys.* **41**, 3144 (1970).
- [12] L. Boshoff-Mostert and H. J. Viljoen, *J. Appl. Phys.* **86**, 1245 (1999).
- [13] Q. Wu and F. Jing, *Appl. Phys. Lett.* **67**, 49 (1995).
- [14] Q. Wu and F. Jing, *J. Appl. Phys.* **80**, 4343 (1996).
- [15] H. Geng, Q. Wu, H. Tan, L. Cai and F. Jing, *J. Appl. Phys.* **92**, 5924 (2002).
- [16] P. Erhart, E. M. Bringa, M. Kumar, and K. Albe, *Phys. Rev. B* **72**, 052104 (2005).
- [17] Q. Yang, G. Zhang, A. Xu, Y. Zhao, Y. Li, *Acta Phys. Sini.* **57**, 940 (2008).
- [18] X. F. Pan, A. Xu, G. Zhang, et al, *Commun. Theor. Phys.* **49**, 1129 (2008).
- [19] X. F. Pan, A. Xu, G. Zhang and J. Zhu, *J. Phys. D: Appl. Phys.* **41**, 015401 (2008).
- [20] A. Xu, X. F. Pan, G. Zhang and J. Zhu, *J. Phys.: Condens. Matter* **19**, 326212(2007).
- [21] A. Xu, G. Zhang, X. F. Pan, J. Zhu, *Commun. Theor. Phys.* **51**, 691 (2009).
- [22] A. Xu, G. Zhang, X. F. Pan, P. Zhang and J. Zhu, *J. Phys. D: Appl. Phys.* **42**, 075409 (2009).
- [23] A. Xu, G. Zhang, P. Zhang, X. F. Pan, J. Zhu, *Commun. Theor. Phys.* **52**, 901 (2009).
- [24] Y. Jiang and M. Liu, *Phys. Rev. Lett.* **99**, 105501 (2007); A. Xu, G. Zhang, H. Li and J. Zhu *Chin. Phys. Lett.* **27**, 026201 (2010).
- [25] H. Minkowski, *Mathematische Annalen*, **57** 447(1903).
- [26] K. R. Mecke, *Int. J. Mod. Phys. B* **12**, 861 (1998).
- [27] Hubert Mantz, Karin Jacobs and Klaus Mecke, *J. Stat. Mech.* P12015 (2008).

- [28] K. R. Mecke, Phys. Rev. E **53**, 4794 (1996).
- [29] K. R. Mecke and V. Sofonea, Phys. Rev. E **56**, R3761 (1997).
- [30] A. Aksimentiev, Krzysztof Moorthi and R. Holyst, J. Chem. Phys. **112**, 6049 (2000).
- [31] P. Cabella, F. Hansen, D. Marinucci, D. Pagano and N. Vittorio, Phys. Rev. D **69**, 063007 (2004).
- [32] G. J. A. Sevink and A. V. Zvelindovsky, J. Chem. Phys. **121**, 3864 (2004)
- [33] S. Rehse, K. Mecke, R. Magerle, Phys. Rev. E **77**, 051805 (2008).
- [34] C. H. Arns, M. A. Knackstedt and K. R. Mecke, Phys. Rev. Lett. **91**, 215506 (2003).
- [35] H. Hadwiger, Abh. Math. Sem. Univ. Hamburg **20**, 136 (1956); Math. Z. **71**, 124 (1959).
- [36] V. Sofonea, et al, Eur. Phys. J. B **8**, 99 (1999).
- [37] In our previous paper[22], the porosity is described by the ratio $\delta = \rho_0/\rho$. The relation between Δ and δ is $\Delta = 1 - 1/\delta$. The larger δ is, the larger Δ is.

This figure "Fig1.jpg" is available in "jpg" format from:

<http://arxiv.org/ps/1005.0908v1>